Topological vortex mode for flexural waves in pillared plates

Zhihui Wen, Julio Andrés Iglesias Martínez, Yabin Jin, Yan Li, Bahram Djafari-Rouhani, Daniel Torrent, Jean-Louis Raynaud, Abdelkrim Khelif

Materials & Design 233 (2023) 112209

Contents lists available at ScienceDirect

Materials & Design

journal homepage: www.elsevier.com/locate/matdes

Topological vortex mode for flexural waves in pillared plates

Zhihui Wen [a,c,1], Julio Andrés Iglesias Martínez [b,1], Yabin Jin [a,*], Yan Li [a], Bahram Djafari-Rouhani [d], Daniel Torrent [c], Jean-louis Raynaud [b], Abdelkrim Khelif [b,e,*]

[a] School of Aerospace Engineering and Applied Mechanics, Tongji University, Shanghai 200092, PR China
[b] Institut FEMTO-ST, CNRS, Université de Bourgogne Franche-Comté, 15B Avenue des Montboucons, CEDEX, F-25030 Besançon, France
[c] GROC-UJI, Institut de Noves Tecnologies de la Imatge, Universitat Jaume I, 12080 Castello, Spain
[d] Institut d'Electronique, de Microélectonique et de Nanotechnologie, UMR CNRS 8520, Département de Physique, Université de Lille, 59650 Villeneuve d'Ascq, France
[e] CINTRA, IRL 3288, CNRS/NTU/Thales, Research Techno Plaza, 50 Nanyang Drive, Singapore, 637553, Singapore

ARTICLE INFO

Keywords:
Topological vortex mode
Flexural waves
Pillared plates
Robustness
Resonant sensing

ABSTRACT

Localized topological modes with high robustness to various perturbations are receiving increasing attention. Recently, zero-order topological vortex modes have been designed in phononic structures, in analogy with zero-energy fermionic states modulated by Jackiw-Rossi binding mechanism. Such localized modes may have potential applications for biosensing, bioimaging and on-chip communication. In this work, we propose a pillared phononic plate with a Kekulé distortion of pillars position to bind topological modes at a vortex core via dispersion engineering. The phase winding and amplitude diagrams of the topological vortex mode are observed experimentally. It is found that existence of vibration peaks and corresponding mode patterns are strongly robust against the random perturbation of resonant frequencies of pillars at the vortex core. We further design a topological resonant sensor for mass sensitivity. The frequency of the topological vortex mode is almost linearly sensitive to added small mass at the vortex core in terms of mass values and positions. The proposed pillared plates provide a platform for potential applications such as energy localization and harvesting, remote health monitoring.

1. Introduction

In the field of topological matter, a great deal of current interest is focused on the study of localized modes for artificial manipulations in various applications such as synthetic dimensional topological insulator [1], Moiré lattices [2–4], topological Anderson insulators [5–7] and so on. The traditional localized modes (e.g., cavity mode) constructed by removing scatterers in artificial structures are widely used for wave-guiding and demultiplexing phenomena [8,9], slow wave velocities [10,11], high-density energy harvesting [12,13], among others. However, these modes are very sensitive to the precise geometric parameters and their performance can be altered by random perturbations in actual manufacturing and operating processes [14,15].

Conversely, localized modes with topological character could provide strong robustness against various perturbations [16–22]. The achievement of topological phases allows for unprecedented manipulation of waves, such as Non-Hermitian skin modes [23–25], topological insulators [16,26–28], Weyl semimetals [29–31] and topological disclination states [32–35]. Particularly, the zero-dimensional topological systems could be used for sensing, energy capture or on-chip communications. Intriguingly, the Jackiw-Rossi model [36] allowed to construct a zero-dimensional localized topological fermionic state at the core of a vortex-fermion system, which is similar to paired fermion states in p-wave superconductors [37]. The equivalent localized zero modes could be trapped when the phase and mass of Dirac fermions are subject to a Kekulé distortion [38]. Inspired by the Jackiw–Rossi model, analogous topological photonic and phononic localized modes [39–47] originated from intervalley coupling and defined by Kekulé distortion have been designed and allow to achieve zero-dimensional optical, acoustic and elastic modes. Recently, Kekulé distortion was used to achieve the degenerate topological states bind to disclinations [39].

In particular, to trap an elastic topological vortex mode, a model of mass-neck spring resonators on a plate (mimicking the case of pillared phononic crystals) associated with the Kekulé distorsion of their positions has been developed [48]. Then, its functional application to energy harvesting has been investigated [49]. The high energy density resulting

* Corresponding authors.
E-mail addresses: 083623jinyabin@tongji.edu.cn (Y. Jin), abdelkrim.khelif@femto-st.fr (A. Khelif).
[1] Equal contribution.

https://doi.org/10.1016/j.matdes.2023.112209
Received 28 December 2022; Received in revised form 23 July 2023; Accepted 31 July 2023
Available online 7 August 2023

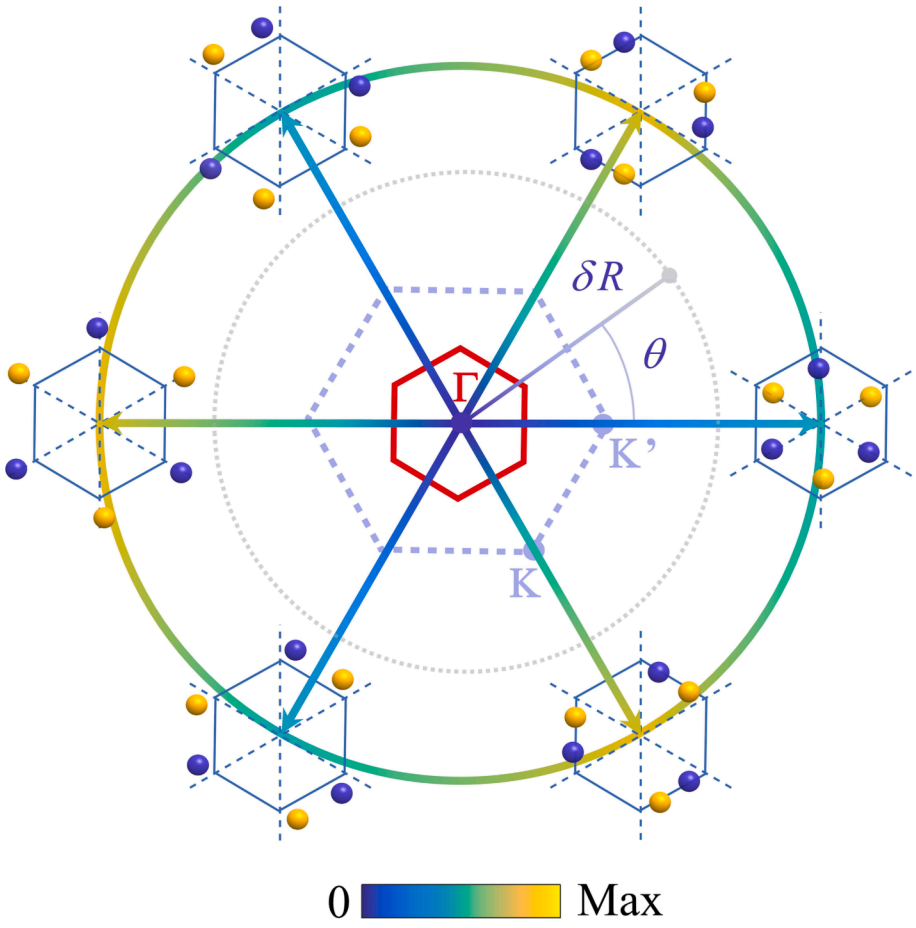

Fig. 1. Mechanism of the topological vortex with position-dependent Kekulé distortion. The color band along with δR is to illustrate the opening of the bandgap with the winding number $n = 1$. The circle color band demonstrates the evolution process of bandgap width modulated by Kekulé phase θ. The minimal bandgaps at $\theta = 0$, $2\pi/3$ and $4\pi/3$ show a periodicity of $2\pi/3$. The outside six honeycomb supercells give the position-dependent of scatterers (blue and yellow dots) with Kekulé distortion, which explains that the common bandgap is $2\pi/3$ based on identical geometric supercells.

from the localization enhancement associated with this topological vortex mode may be used for biosensing [50], bioimaging [51,52] and on-chip communication [53]. The mass-neck spring resonators can be well described with the multiple scattering theory [48,49], however, the complex geometry of resonators hinders the potential applications especially at micro/nano scale for compact and integrated devices. Pillared resonators play an important role in discovering rich physics of different vibrating modes [54]. Compared to the hole scatterers [41], the pillared resonators provide an additional freedom to manipulate the elastic waves especially with subwavelength pillar's size. Although the shape is simply cylindric, pillared resonators have diverse vibrational properties and neighboring coupling effects [54,55], making them unpredictable with an analytical theory model at the moment. Meanwhile, the vortex mode can be expanded in anisotropic media [56] and furthermore could be designed in other shapes such as in Laguerre-Gaussian beams [57,58] or with the fractional topological charge [59]. It is therefore necessary to reveal how to realize topological vortex modes with pillared resonators.

In this work, we propose cylindrical pillars to construct the zero-dimensional topological vortex mode in a phononic plate. We first design the topological vortex modes by engineering the dispersion of the pillars. The vortex phase and topological peak are numerically and experimentally validated. We then exhibit the robust behavior of topological vortex modes as a function of the randomness of pillars' resonant frequencies which may be induced in geometrical or material parameters from actual manufacturing and operating processes. Furthermore, a topological resonator mass sensor is proposed regarding the value and position of the mass. Finally, we make a summary of this work.

2. Principles of the Jackiw-Rossi binding mechanism

The Jackiw-Rossi model [36] constructs a vortex-fermion system that sustains localized topological fermionic states at vortex core. The Jackiw-Rossi binding mechanism of such vortex states is similar to paired fermion states in p-wave superconductors [37] modulated by breaking the parity and time-reversal symmetries that is defined as Majorana bound state. The equivalent zero mode was trapped in graphene lattice by a twist in the phase and mass of Dirac fermions, which is called Kekulé distortion [38].

Analogous to the Jackiw-Rossi binding mechanism, vortices supporting localized zero-mode have been designed in optic [43,44] and acoustic [39,46] clusters by means of a Kekulé distortion. It could be preferable to apply the distortion to the position of the scatterers (pillars in our case) rather than to their geometrical parameters such as height or radius. We start from a honeycomb lattice with its Brillouin zone (BZ) presented by blue-dashed lines in Fig.1. Such a lattice displays Dirac cones at the K and K' valleys of BZ. A uniform deformation of the lattice gives rise to a bigger unit cell and hence a smaller BZ (red lines in Fig. 1) where the initial K and K' points are folded to the Γ point in [50]. Finally, the Kekulé deformation will be at the origin of a complex valley modes hybridization which leads to a band gap opening and trapping of the vortex mode. The honeycomb supercell could be considered as a double C_{3v}-symmetric system, as shown by the yellow and blue solid dots in Fig. 1. The position-dependent Kekulé distortion with phase winding can be formulated as

$$\vartheta(r,\theta) = \delta R(r)\cdot(-i\varphi)e^{-i\varphi(k\cdot r+\phi)}, \tag{1}$$

The distorted lattice can be defined as $(r_x+\mathrm{Re}\vartheta, r_y+\mathrm{Im}\vartheta)$, where $\delta R(r) = R_0\tanh(|r|/w)$ modulates the bandgap open process with distortion

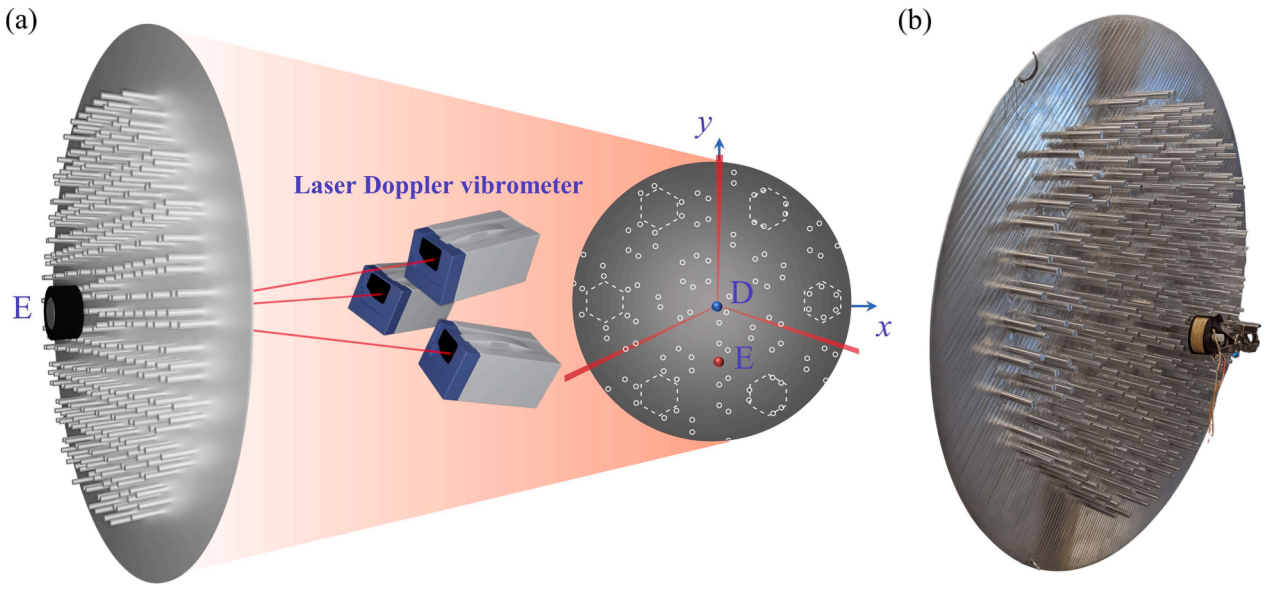

Fig. 2. Experimental setup. (a) Sketch of experimental device with the excitation magnet E at the front side and the detection D at the back side captured by laser Doppler vibrometer, in which the point D is also the vortex core and the orign point in. (b) Pillared phononic plate sample for experimental observation of topological vortex modes. The magnetic excitation source is set near the center of the sample at point $(0, -a)$.

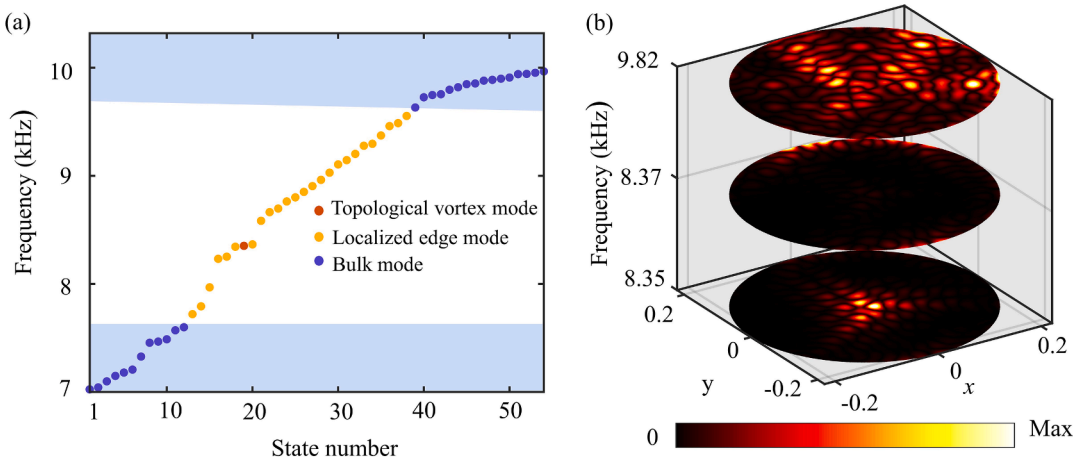

Fig. 3. Eigenmode simulations of topological vortex mode. (a) Eigenfrequencies of a finite pillared cluster cover the common bandgap from 7.63 kHz to 9.69 kHz exhibited by white zone with radius $R = 0.2208$ m. (b) The out-of-plane patterns of the topological vortex mode at 8.35 kHz (red solid dot in panel a), traditional localized edge mode at 8.37 kHz (orange solid dots) in the common bandgap and the bulk mode at the 9.82 kHz (blue solid dots) in the light-blue zone.

amplitude $R_0 = 0.12a/\sqrt{3}$ and vortex radius $w = 0.1a/\sqrt{3}$, φ corresponds to the double C_{3v}-symmetric system and equals 1 and -1 for yellow and blue C_{3v}-symmetric pillars, respectively. The Kekulé wavevector is fixed to $\boldsymbol{k} = [4\pi/\sqrt{3}\,a, 0]$, $\boldsymbol{r}$ is the undistorted position vector of pillars and a is the supercell lattice constant (See geometric parameters in methods). Importantly, the winding phase $\phi = n\theta$ embodies a topological pumping for trapping the vortex mode [60]. Here the winding number n is set to be 1. The circle color band demonstrates the evolution process of bandgap width modulated by Kekulé phase θ. The dispersion curves of narrowest or widest bandgaps can be found in Appendix A. Both the narrowest bandgaps at $\theta = 0$, $2\pi/3$ and $4\pi/3$ and widest bandgaps at $\theta = \pi/3$, π and $5\pi/3$ reveal a clearly $2\pi/3$ periodic repetition. The distorted supercells at narrowest or widest bandgaps have essentially the same geometric structures, except for different selection methods, which illustrates the periodicity of common bandgap. Around the center, we have $\delta R = 0$, and the gapless core (as can be seen by the dark blue color in Fig. 1) eventually captures a topological vortex. Such bandgap pattern modulated by position-dependent Kekulé distortion could construct the topological vortex mode, also called topological mid-gap state.

To excite the topological vortex mode and observe the phase winding, we proposed the experimental device shown in Fig. 2(a). We manufacture the pillared phononic plate sample made of Aluminum based on integrated milling machines and standard material parameters (See simulation and fabrication in methods). The magnetic excitation source E is put in front of the pillared phononic plate to imitate an approximate point source for exciting the topological vortex mode for flexural waves in the plate at point $(0, -a)$. Three axis laser Doppler vibrometer at the back-side scans the out-of-plane displacements of the detection D (See measurement in methods). The whole metal sample is suspended by quadrangular symmetrical metal rings and existed by a magnetic coil as shown in Fig. 2(b).

3. Validation of the topological vortex mode

The simulated eigenfrequencies and selected representative

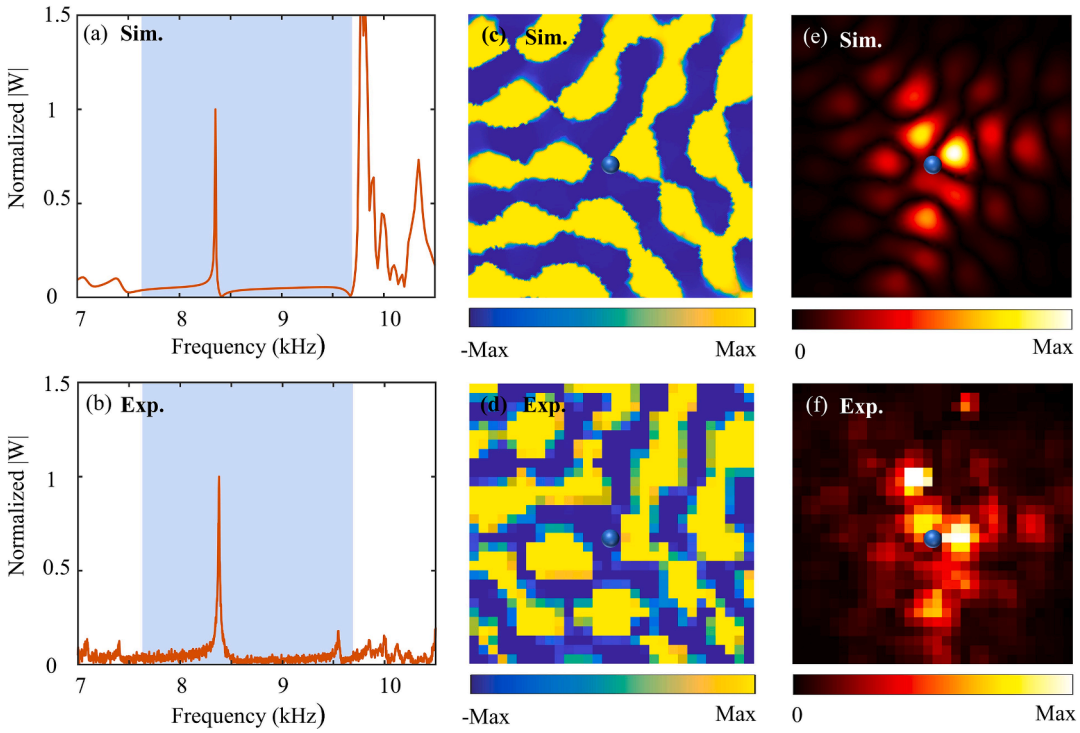

Fig. 4. Experimental observation of topological vortex modes. (a) Simulated (Sim.) and (b) experimental (Exp.) response spectra normalized by the topological peaks at 8352 Hz (Sim.) and 8375 Hz (Exp.) at the point of vortex core (blue ball in (c-f)), respectively. Quality factors of the topological peaks are $Q_{Sim.} = 588.2$ and $Q_{Exp.} = 271.5$. The Experimental setup is the same as in Fig. 2 and magnetically excited at point $(0, -a)$. The blue zones in (a, b) are the common bandgaps. Normalized patterns of phases (c, d) and out-of-plane displacements (e, f) of the topological vortex mode measured within the range of −10 to 10 cm of x- and y-axes at topological frequencies 8352 Hz (Sim.) and 8375 Hz (Exp.), respectively.

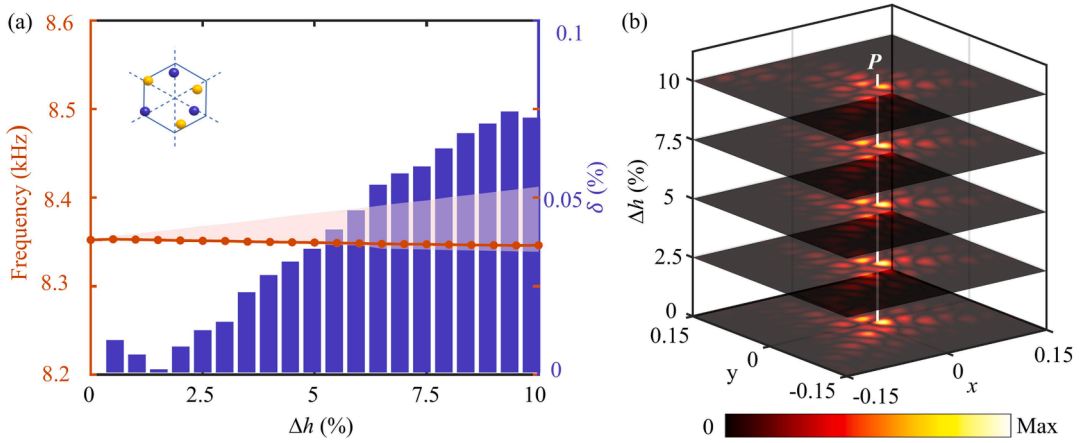

Fig. 5. Robustness of the topological vortex mode. (a) The robustness of maximal height random disturbance Δh of the scatterers at vortex core. The left and right axes of the double y axis are frequencies of topological peaks and their error δ under the random disturbance Δh, respectively. (b) Patterns of topological peaks with height random disturbance $\Delta h = 0$, 2.5%, 5%, 7.5% and 10%, respectively. The point P is the max value of the pattern at topological peak with $\Delta h = 0$.

eigenmodes about the part of the finite phononic plate in Fig. 2(b) with pillars are shown in Fig. 3. The light-blue and white zones indicate the bulk band and common bandgap in Fig. 3(a), respectively. Based on our expected design with position-dependent Kekulé distortion, the topological vortex mode appears at 8.352 kHz. In the common bandgap, there are many traditional localized edge modes due to the existence of boundaries of the finite structure, which is identical to edge states in a triangular acoustic structure [61]. In Fig. 3(b), the topological vortex eigenmode clearly bounds to the vortex core at 8.352 kHz and highlights spots (displacement peaks) around the vortex core. For traditional edge states such as at 8.37 kHz, the displacement at the center of the plate is almost zero, which allows us to experimentally observe the topological vortex mode. We also show the example of the trivial bulk mode at 9.82 kHz in Fig. 3(b) whose displacement spreads over the plate. The vortex mode is highly localized in a small domain around the vortex core and does not extend to the boundary of the structure. It will remain even unaffected if the size of the sample is increased in the simulation. For this reason, the simulation has been performed by assuming free boundary conditions and this reproduces very well of the experimental results even the effective sample is hanged at its corner.

Experimental validation of the excited topological vortex mode is carried out and compared with numerical simulation in Fig. 4 (See the simulation and measurement in Methods). The blue zone indicates the common bandgaps in Fig. 4(a) and (b). Topological peaks in common

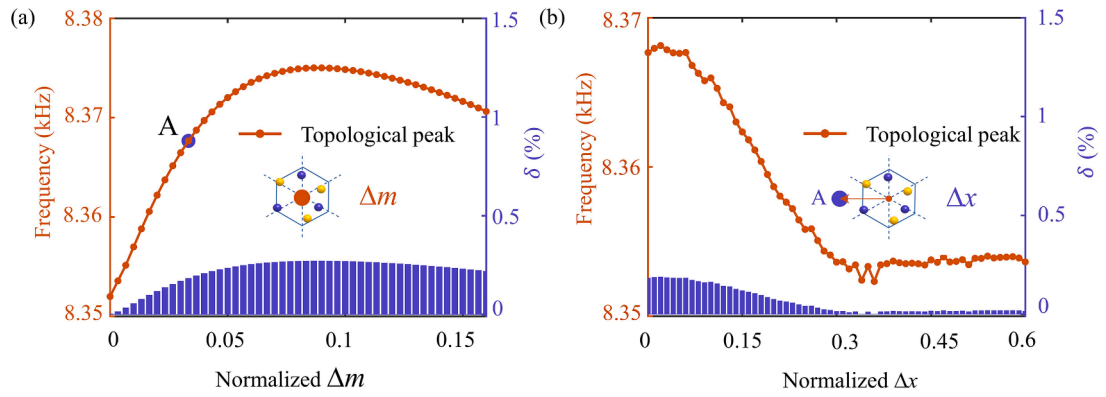

Fig. 6. The influence of added objects on the topological vortex modes as a function of (a) normalized mass Δm at vortex core (as shown in the inset) and (b) normalized deviated position away from vortex core center Δx (as shown in the inset). The normalized mass Δm_A is the same as point A in panel (a), and the right axes of the double y axis are the error δ of topological peaks in (a) and (b), respectively.

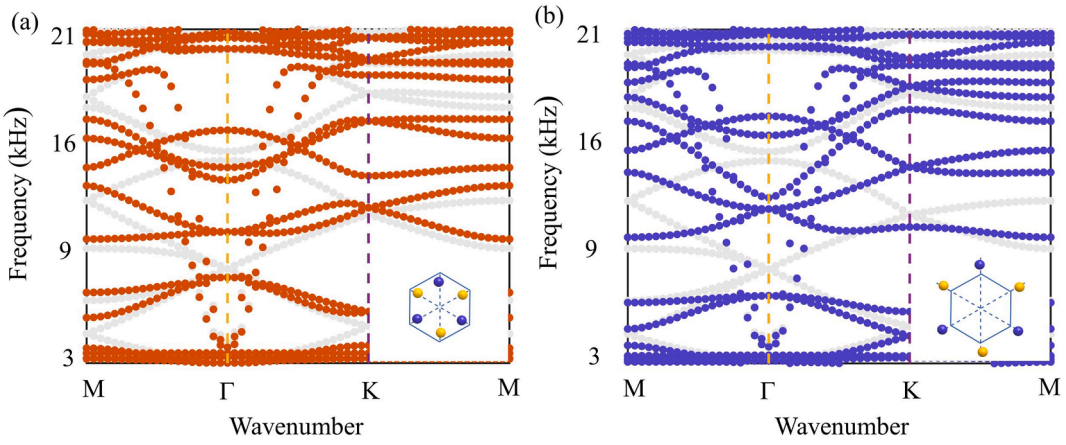

Fig. S1. The classical double Dirac cone at Γ point (Grey bands) before Kekulé distortion and (a) the narrowest and (b) the widest bandgaps opened after the distortion and delimited respectively by the orange and blue dispersion curves. The insets in (a) and (b) show unit cells with six pillared scatterers of the narrowest and widest bandgaps, respectively.

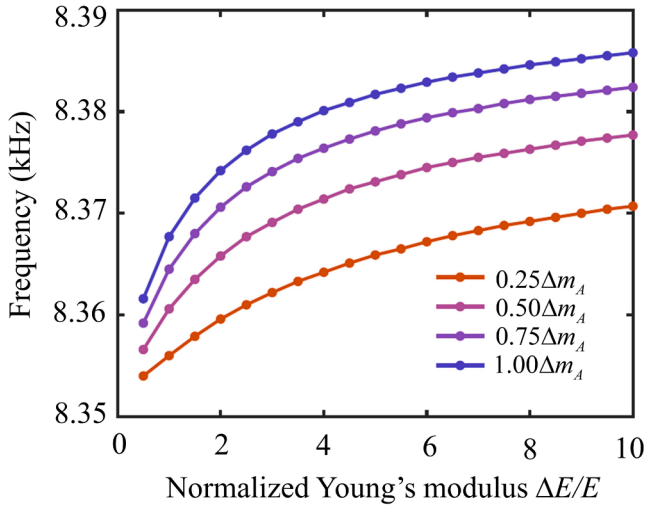

Fig. S2. The sensing of Young's modulus, where E is the Young's modulus of the aluminum alloy.

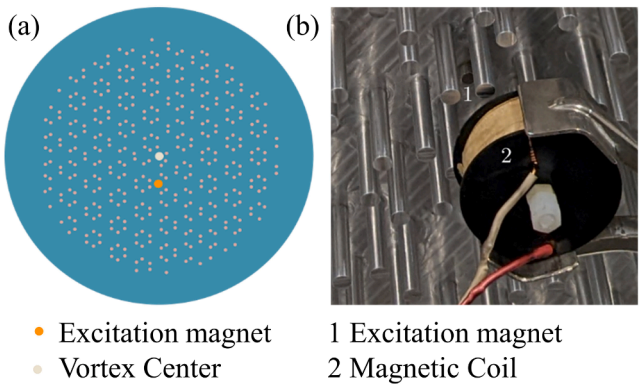

Fig. S3. (a) Position of the vortex center and excitation magnet. (b) Photograph of the magnet and magnetic coil in the sample for Lamb wave excitation.

bandgaps are observed at f_{ts} = 8352 Hz in simulation (Sim.) and f_{te} = 8375 Hz in experiment (Exp.) with a negligible error $|(f_{ts} - f_{te})/f_{ts}|$ = 0.27%, which shows an excellent consistence. The topological vortex mode has an extra sharp peak with a high-quality factor $Q = f_p/\Delta f_p$, where f_p and Δf_p are the peak value and the width of midfrequency of the vortex mode, respectively. The quality factors of topological peaks are $Q_{Sim.}$ = 588.2 and $Q_{Exp.}$ = 271.5 that reveals the quality factor of the vortex mode can be affected by manufacturing and operating conditions but still achieve a high value in practice. Interestingly, the trivial peak above the upper frequency limit of the common bandgap in simulation in Fig. 4(a) doesn't appear in the experimental response curve in Fig. 4

(b), which further supports the importance of robustness of topological mode.

To validate the formation of a vortex mode, simulated and experimental displacement phase and amplitude patterns are also captured in Figs. 4(c-f) around the vortex core (blue ball in (c-f)), which is the original point of the Kekulé distortion. From Figs. 4(c) and (d), both of the simulated and experimental displacement phase patterns have continuous positive and negative phase alternation and shape the phase winding in the vortex core with a periodicity of $2\pi/3$, which reveals the formation mechanism of a vortex mode and drives finally displacement patterns. From Figs. 4(e) and (f), the displacement patterns at topological frequencies f_{ts} and f_{te} show an excellent agreement, which could provide an effective and robust platform for wave function modulation with pillared phononic crystals. The robustness of the vortex mode frequency against disorder in the sample will be discussed in the next section. Here, we would notice that our work is a necessary step towards the technological design of samples at the microscale for operation at high frequencies. Indeed, in the latter case, the position and diameter of the pillars can be effectively controlled through the mask process at the microscale, while managing their heights poses a greater challenge, as it requires halting the film deposition. In the current configuration, the pillars are welded to the plate using laser welding, which can introduce an error in the final height of approximately 1 to 2%. This error is equivalent to the inaccuracies encountered during the growth process at the microscale, particularly when utilizing the electroplating technique, especially for high aspect ratio structures like ours.

4. Robustness of the topological vortex modes

The gapless (see Fig. 1) at the vortex core constructs the vortex modes. The resonant frequencies of the pillars at the vortex core, which mainly effected by the high of the pillar, the gapless will be modulated by the pillars at the vortex core. To verify the robustness of the topological vortex mode, we numerically focus on the random perturbation of pillars' resonant frequencies at the vortex core, which have the highest ability of affecting the vortex mode via constructing the asymmetric random perturbation at the vortex core [46,48,49]. The random disturbance of height Δh could lead to the disturbance of resonant frequencies of the six scatterers at the vortex core, resulting in breaking the symmetry of vortex core in the pillared phononic plate. We present the topological vortex mode frequencies and the corresponding frequency deviations $\delta = |f_{\Delta h} - f_t|/|f_t|$ in Fig.5(a), where the average frequency $f_{\Delta h} = 1/n\sum f_{\Delta h(n)}$ is the average values of topological peaks with random perturbations of height $\Delta h(n)$ and $n = 20$. The light pink triangle area surrounding the average frequency response curve gives the boundary of the frequency deviation with random perturbations of height $\Delta h(n)$. The corresponding average frequency deviations are still <0.1 %, even if the maximum frequency deviation does not exceed 0.7%, showing strong robustness of the topological vortex mode. In Fig. 5(b), we present five displacement patterns of the topological vortex mode for different Δh and the point P is the max value of the displacement at $\Delta h = 0$. One can note that all illustrations exhibit stable and robust vortex mode patterns.

Resonant sensing such as mass sensors [62–64] is very important for remote monitoring of changes in mechanical environment. We now put an object with mass m at the vortex core and define the normalized object's mass as $\Delta m = m/m_R$, where m_R is the mass of a single pillar. The corresponding maximal frequency deviations $\delta_{\Delta m} = |f_{\Delta m} - f_t|/|f_t| < 0.27\%$ and $\delta_{\Delta x} = |f_{\Delta x} - f_t|/|f_t| < 0.19\%$ reveal that topological modes are strongly robust against added objects. Interestingly, the frequency of the topological vortex eigenmode first increases linearly when the added object Δm is < 0.05 due to the stiffness contribution of added mass see Appendix B. Then it continuously increases to a maximum value when $\Delta m = 0.08$, and decreases slightly afterwards, as shown in Fig. 6(a). After some points ($\Delta m = 0.08$ in the above arrangement), the mass of the added object has a dominant role, the frequency of topological modes decrease with the increase of the added mass. We further select a normalized mass $\Delta m_A = 1/30$ and present the frequency as a function of the added object's positions $\Delta x = x/a$ in Fig. 6 (b), where x is the deviated position from the center and a is the honeycomb lattice constant. It is observed that the frequency first keeps stable when $\Delta x < 0.06$ then it decreases almost linearly when Δx is smaller than 0.3, afterwards it remains unchanged. Meanwhile, the competition between the Young's modulus and the mass is also an interesting topic, this point is discussed in Appendix B. The frequencies increase with the increasing of the normalized Young's modulus. The variation of the frequency of the topological vortex eigenmode reveals that the vortex core plays important role in the topological vortex mode and it is sensitive to added small-mass objects which could have a potential application for the biological cell sensing at nano scale.

5. Summary

We numerically designed and experimentally validated the topological vortex mode in phononic plates with pillared resonators by engineering the dispersions. The displacement phase and amplitude patterns of the topological vortex mode agree well between the numerical and experimental results. Considering the inevitable and random perturbations of pillars' material or geometric parameters in practice which result in a deviation in pillar's resonant frequency, we studied the influence of random height perturbation in pillars on the topological vortex eigenmodes and showed strong robustness in displacement patterns. Furthermore, the topological vortex mode is very sensitive to small-mass objects in the predictable frequency range in terms of mass and position, which could facilitate the design of resonant sensors. The proposed pillared plates with topological vortex modes can be used for energy localization and harvesting, remote health monitoring, signal processing, et al.

Declaration of Competing Interest

The authors declare that they have no known competing financial interests or personal relationships that could have appeared to influence the work reported in this paper.

Data availability

Data will be made available on request.

Acknowledgements

This work was supported by the National Natural Science Foundation of China (No. 12272267, No. 11902223), the Young Elite Scientists Sponsorship Program by CAST(2021QNRC001), the Shanghai Science and Technology Committee (No. 21JC1405600, 22JC1404100), the program for professor of special appointment (Eastern Scholar) at Shanghai Institutions of Higher Learning, the Fundamental Research Funds for the Central Universities. This work was also supported by the EIPHI Graduate School and the French National Research Funding agency (Contract No. "ANR-17-EURE-0002"). Zhihui Wen acknowledges a scholarship provided by the China Scholarship Council (No. 202106260070). The authors also thank Prof. Penglin Gao for fruitful discussion.

Appendix A:. Band structures of supercells

To show bandgap width modulated by Kekulé phase θ, we calculated the dispersion curves of the narrowest in Fig. S1 (a) and widest bandgap in Fig. S1 (b) with the Kekulé phase $\theta = \kappa\pi/3$ (κ=0,2,4) and $\theta = \kappa\pi/3$ (κ=1,3,5). Grey dispersion curves show a clear double Dirac cone. Topological vortex modes originated from intervalley coupling and defined by Kekulé distortion will appear in the opened gap at the Dirac frequency.

Appendix B:. The sensing for the mass and rigidity of added objects

Different materials have different specific parameters and the Young's modulus cannot be continuous, so we chose the Young's modulus of aluminum alloy in the main text. Meanwhile, the competition between the mass and the rigidity of the added object is also important to reveal the sensing of Young's modulus. we investigated the sensing of the Young's modulus in Fig. S2, where the Δm is kept below$\Delta m_A$to remain in the linearly range of Fig. 6(a). We can see that the frequencies increase with the increasing of the normalized Young's modulus for different Δm. For Δm, it is still following the phenomenon as shown in the main text.

Methods

Simulation

We use COMSOL Multiphysics with MATLAB to simulate the response spectra, phases and out-of-plane patterns of the full-scale pillared phononic plate model that contains the topological vortex mode. The geometric parameters of the pillared phononic plate are lattice constant $a = 50$ mm, height and radius of pillars $h = 30$ mm and $r = 3$ mm, respectively. The material parameters of aluminum alloy are Young's modulus $E = 71$ GPa, Poisson's ratio $\upsilon = 0.33$, density $\rho = 2730$ kg/m^3. The simulated process is Geometry model, Material settings, Solid Mechanics settings and study under given or desired number of eigenfrequencies around a set frequency. The ring-shaped perfectly matched layer was chosen to avoid reflection for calculating response spectra. To obtain high-precision simulation solutions and improve computing efficiency, the top surface of pillars and plates were meshed by free triangular elements, and swept under appropriate sizes. The meshed models contained about 6.27 and 6.42 million degrees of freedom for calculating of eigenstates and response spectra in frequency domain. The average element qualities of both models are larger than 0.77.

Fabrication and measurement

The sample is fabricated in its totality in aluminum, by soldering pre-machine rods into a pre-machine plate (by Facturee®). Each road with a length of 30.0 mm and with a diameter of 6.0 mm. The plate has a circular geometry with a diameter of 541.7 mm and a thickness of 2 mm. Four holes are distributed like a square at the corners of sample where made, to hang it from the celling with the help of wire steel, and the two bottom holes to the floor without tension on them, for the positioning of the sample.

To generate the Lamb waves a magnet, with 5 mm of diameter and 5 mm of thickness, is located as it shows in the Fig. S3 (a) and glued with some cyanoacrylate adhesive. A Magnetic Coil (electromagnet) with an iron core is as close as possible, Fig. S3 (b). To get the full spectrum response, a periodic chirp signal, with the bandwidth from 4 kHz to 12 kHz is used as input signal, then amplified with a power amplifier (Brüel & Kjær Type 2706) and connected to the electro-magnet. The out of plane displacement from the back part (with no pillars) of the sample is recorded with the help of a doppler vibrometer, PSV-500-3D, perpendicular to the surface and scanned for the specific area of interest.

References

[1] E. Lustig, S. Weimann, Y. Plotnik, Y. Lumer, M.A. Bandres, A. Szameit, M. Segev, Photonic topological insulator in synthetic dimensions, Nature 567 (7748) (2019) 356–360.

[2] P. Wang, Y. Zheng, X. Chen, C. Huang, Y.V. Kartashov, L. Torner, et al., Localization and delocalization of light in photonic moire lattices, Nature 577 (2020) 42–46.

[3] Yabin Jin, Wan Wang, Zhihui Wen, Daniel Torrent, Bahram Djafari-Rouhani. Topological states in twisted pillared phononic plates. Extreme Mechanics Letters. 2020;39:100777.

[4] Oudich M, Deng Y, Jing Y. Twisted pillared phononic crystal plates. Applied Physics Letters. 2022;120:232202.

[5] S. Stützer, Y. Plotnik, Y. Lumer, P. Titum, N.H. Lindner, M. Segev, M.C. Rechtsman, A. Szameit, Photonic topological Anderson insulators, Nature 560 (7719) (2018) 461–465.

[6] X. Cui, R.-Y. Zhang, Z.-Q. Zhang, C.T. Chan, Photonic $\mathbb{Z}_2$ Topological Anderson Insulators, Phys. Rev. Lett. 129 (2022), 043902.

[7] W. Zhang, D. Zou, Q. Pei, W. He, J. Bao, H. Sun, X. Zhang, Experimental observation of higher-order topological Anderson Insulators, Phys. Rev. Lett. 126 (14) (2021), 146802.

[8] Y. Jin, N. Fernez, Y. Pennec, B. Bonello, R.P. Moiseyenko, S. Hémon, Y. Pan, B. Djafari-Rouhani, Tunable waveguide and cavity in a phononic crystal plate by controlling whispering-gallery modes in hollow pillars, Phys. Rev. B 93 (5) (2016), 054109.

[9] Y. Jin, B. Djafari-Rouhani, D. Torrent, Gradient index phononic crystals and metamaterials, Nanophotonics. 8 (2019) 685–701.

[10] S.-Y. Yu, J.-Q. Wang, X.-C. Sun, F.-K. Liu, C. He, H.-H. Xu, M.-H. Lu, J. Christensen, X.-P. Liu, Y.-F. Chen, Slow surface acoustic waves via lattice optimization of a phononic crystal on a chip, Phys. Rev. Appl 14 (6) (2020), 064008.

[11] Ma T-X, Fan Q-S, Zhang C, Wang Y-S. Acoustic flatbands in phononic crystal defect lattices. Journal of Applied Physics. 2021;129:145104.

[12] Ma K, Tan T, Yan Z, Liu F, Liao W-H, Zhang W. Metamaterial and Helmholtz coupled resonator for high-density acoustic energy harvesting. Nano Energy. 2021; 82:105693.

[13] Wen Z, Wang W, Khelif A, Djafari-Rouhani B, Jin Y. A perspective on elastic metastructures for energy harvesting. Applied Physics Letters. 2022;120:020501.

[14] Y. Jin, D. Torrent, B. Djafari-Rouhani, Robustness of conventional and topologically protected edge states in phononic crystal plates, Phys. Rev. B 98 (2018), 054307.

[15] J. Noh, W.A. Benalcazar, S. Huang, M.J. Collins, K.P. Chen, T.L. Hughes, M. C. Rechtsman, Topological protection of photonic mid-gap defect modes, Nat. Photonics 12 (7) (2018) 408–415.

[16] G. Ma, M. Xiao, C.T. Chan, Topological phases in acoustic and mechanical systems, Nature Reviews Physics. 1 (2019) 281–294.

[17] G. Harari, M.A. Bandres, Y. Lumer, M.C. Rechtsman, Y.D. Chong, M. Khajavikhan, D.N. Christodoulides, M. Segev, Topological insulator laser: Theory, Science 359 (6381) (2018).

[18] M.A. Bandres, S. Wittek, G. Harari, M. Parto, J. Ren, M. Segev, D. N. Christodoulides, M. Khajavikhan, Topological insulator laser: Experiments, Science 359 (6381) (2018).

[19] S. Barik, A. Karasahin, C. Flower, T. Cai, H. Miyake, W. DeGottardi, M. Hafezi, E. Waks, A topological quantum optics interface, Science 359 (6376) (2018) 666–668.

[20] M. Maldovan, Sound and heat revolutions in phononics, Nature 503 (7475) (2013) 209–217.

[21] J.-Q. Wang, Z.-D. Zhang, S.-Y. Yu, H. Ge, K.-F. Liu, T. Wu, X.-C. Sun, L.e. Liu, H.-Y. Chen, C. He, M.-H. Lu, Y.-F. Chen, Extended topological valley-locked surface acoustic waves, Nat. Commun. 13 (1) (2022).

[22] H. Zhao, X. Qiao, T. Wu, B. Midya, S. Longhi, L. Feng, Non-Hermitian topological light steering, Science 365 (6458) (2019) 1163–1166.

[23] W. Wang, X. Wang, G. Ma, Non-Hermitian morphing of topological modes, Nature 608 (7921) (2022) 50–55.

[24] Jin Y, Zhong W, Cai R, Zhuang X, Pennec Y, Djafari-Rouhani B. Non-Hermitian skin effect in a phononic beam based on piezoelectric feedback control. Applied Physics Letters. 2022;121:022202.
[25] R. Cai, Y. Jin, Y. Li, T. Rabczuk, Y. Pennec, B. Djafari-Rouhani, X. Zhuang, Exceptional points and skin modes in non-hermitian metabeams, Phys. Rev. Appl 18 (1) (2022), 014067.
[26] M.C. Rechtsman, J.M. Zeuner, Y. Plotnik, Y. Lumer, D. Podolsky, F. Dreisow, S. Nolte, M. Segev, A. Szameit, Photonic Floquet topological insulators, Nature 496 (7444) (2013) 196–200.
[27] S. Yin, E. Galiffi, A. Alù, Floquet metamaterials. eLight. 2 (2022) 8.
[28] Jin Y, He L, Wen Z, Mortazavi B, Guo H, Torrent D, et al. Intelligent on-demand design of phononic metamaterials. Nanophotonics. 2022;11:439-460.
[29] B.Q. Lv, H.M. Weng, B.B. Fu, X.P. Wang, H. Miao, J. Ma, et al., Experimental Discovery of Weyl Semimetal TaAs, Phys. Rev. X 5 (2015), 031013.
[30] L. Lu, Z. Wang, D. Ye, L. Ran, L. Fu, J.D. Joannopoulos, M. Soljačić, Experimental observation of Weyl points, Science 349 (6248) (2015) 622–624.
[31] X. Fan, C. Qiu, Y. Shen, H. He, M. Xiao, M. Ke, Z. Liu, Probing Weyl physics with one-dimensional sonic crystals, Phys. Rev. Lett. 122 (13) (2019), 136802.
[32] Y. Liu, S. Leung, F.-F. Li, Z.-K. Lin, X. Tao, Y. Poo, J.-H. Jiang, Bulk-disclination correspondence in topological crystalline insulators, Nature 589 (7842) (2021) 381–385.
[33] C.W. Peterson, T. Li, W. Jiang, T.L. Hughes, G. Bahl, Trapped fractional charges at bulk defects in topological insulators, Nature 589 (7842) (2021) 376–380.
[34] Y. Chen, Y. Yin, Z.K. Lin, Z.H. Zheng, Y. Liu, J. Li, et al., Observation of topological p-orbital disclination states in non-euclidean acoustic metamaterials, Phys. Rev. Lett. 129 (2022), 154301.
[35] Xia B, Jiang Z, Tong L, Zheng S, Man X. Topological bound states in elastic phononic plates induced by disclinations. Acta Mechanica Sinica. 2022;38:521459.
[36] R. Jackiw, P. Rossi, Zero modes of the vortex-fermion system, Nucl. Phys. B 190 (4) (1981) 681–691.
[37] N. Read, D. Green, Paired states of fermions in two dimensions with breaking of parity and time-reversal symmetries and the fractional quantum Hall effect, Phys. Rev. B 61 (15) (2000) 10267–10297.
[38] C.Y. Hou, C. Chamon, C. Mudry, Electron fractionalization in two-dimensional graphenelike structures, Phys. Rev. Lett. 98 (2007), 186809.
[39] Y. Deng, W.A. Benalcazar, Z.G. Chen, M. Oudich, G. Ma, Y. Jing, Observation of degenerate zero-energy topological states at disclinations in an acoustic lattice, Phys. Rev. Lett. 128 (2022), 174301.
[40] X. Wu, Y. Meng, Y. Hao, R.-Y. Zhang, J. Li, X. Zhang, Topological corner modes induced by dirac vortices in arbitrary geometry, Phys. Rev. Lett. 126 (2021), 226802.
[41] J. Ma, X. Xi, Y. Li, X. Sun, Nanomechanical topological insulators with an auxiliary orbital degree of freedom, Nat. Nanotechnol. 16 (5) (2021) 576–583.
[42] P. Gao, J. Christensen, Topological vortices for sound and light, Nat. Nanotechnol. 16 (5) (2021) 487–489.
[43] J. Noh, T. Schuster, T. Iadecola, S. Huang, M. Wang, K.P. Chen, C. Chamon, M. C. Rechtsman, Braiding photonic topological zero modes, Nat. Phys. 16 (9) (2020) 989–993.
[44] A.J. Menssen, J. Guan, D. Felce, M.J. Booth, I.A. Walmsley, Photonic topological mode bound to a vortex, Phys. Rev. Lett. 125 (2020), 117401.
[45] X. Gao, L. Yang, H. Lin, L. Zhang, J. Li, F. Bo, Z. Wang, L. Lu, Dirac-vortex topological cavities, Nat. Nanotechnol. 15 (12) (2020) 1012–1018.
[46] P. Gao, D. Torrent, F. Cervera, P. San-Jose, J. Sanchez-Dehesa, J. Christensen, Majorana-like zero modes in Kekulé distorted sonic lattices, Phys. Rev. Lett. 123 (2019), 196601.
[47] Z.-D. Zhang, S.-Y. Yu, M.-H. Lu, Y.-F. Chen, Dual-band helical edge states and discrete dirac vortices in solid-state elastic waves, Phys. Rev. Appl 17 (2022), 034029.
[48] Chen CW, Lera N, Chaunsali R, Torrent D, Alvarez JV, Yang J, et al. Mechanical analogue of a Majorana bound state. Advanced materials. 2019;31:e1904386.
[49] Wen Z, Jin Y, Gao P, Zhuang X, Rabczuk T, Djafari-Rouhani B. Topological cavities in phononic plates for robust energy harvesting. Mechanical Systems and Signal Processing. 2022;162:108047.
[50] Y. Xiong, Q. Huang, T.D. Canady, P. Barya, S. Liu, O.H. Arogundade, C.M. Race, C. Che, X. Wang, L. Zhou, X. Wang, M. Kohli, A.M. Smith, B.T. Cunningham, Photonic crystal enhanced fluorescence emission and blinking suppression for single quantum dot digital resolution biosensing, Nat. Commun. 13 (1) (2022).
[51] Y. Wang, G. Ma, G. Gao, J.i. Tao, W. Cao, H. Sun, F. Ma, Y. Zhang, Y. Wei, M. Tian, Bioimaging of dissolvable microneedle arrays: challenges and opportunities, Research 2022 (2022).
[52] C. Wang, X. Chen, L. Wang, M. Makihata, H.-C. Liu, T. Zhou, X. Zhao, Bioadhesive ultrasound for long-term continuous imaging of diverse organs, Science 377 (6605) (2022) 517–523.
[53] X. Zhao, H. Askari, J. Chen, Nanogenerators for smart cities in the era of 5G and Internet of Things, Joule. 5 (6) (2021) 1391–1431.
[54] Jin Y, Pennec Y, Bonello B, Honarvar H, Dobrzynski L, Djafari-Rouhani B, et al. Physics of surface vibrational resonances: pillared phononic crystals, metamaterials, and metasurfaces. Reports on Progress in Physics. 2021;84:086502.
[55] Y. Jin, B. Bonello, R.P. Moiseyenko, Y. Pennec, O. Boyko, B. Djafari-Rouhani, Pillar-type acoustic metasurface, Physical Review B. 96 (10) (2017), 104311.
[56] T. Fadeyeva, Y.u. Egorov, A. Rubass, G.A. Swartzlander, Jr., A. Volyar, Indistinguishability limit for off-axis vortex beams in uniaxial crystals, Opt. Lett. 32 (21) (2007) 3116.
[57] A. Volyar, M. Bretsko, Y. Akimova, Y. Egorov, Digital sorting perturbed Laguerre-Gaussian beams by radial numbers, J. Opt. Soc. Am. A Opt. Image Sci. Vis. 37 (2020) 959–968.
[58] A. Volyar, E. Abramochkin, Y. Egorov, M. Bretsko, Y. Akimova, Fine structure of perturbed Laguerre-Gaussian beams: Hermite-Gaussian mode spectra and topological charge, Appl. Opt. 59 (2020) 7680–7687.
[59] A.V. Volyar, Y.A. Egorov, Super pulses of orbital angular momentum in fractional-order spiroid vortex beams, Opt. Lett. 43 (2018) 74–77.
[60] P. Gao, J. Christensen, Topological sound pumping of zero-dimensional bound states, Advanced Quantum Technologies. 3 (9) (2020) 2000065.
[61] H. Xue, Y. Yang, F. Gao, Y. Chong, B. Zhang, Acoustic higher-order topological insulator on a kagome lattice, Nat. Mater. 18 (2) (2019) 108–112.
[62] J. Ji, Y. Pang, D. Li, Z. Huang, Z. Zhang, N. Xue, Y.i. Xu, X. Mu, An aptamer-based shear horizontal surface acoustic wave biosensor with a CVD-grown single-layered graphene film for high-sensitivity detection of a label-free endotoxin, Microsyst. Nanoeng. 6 (1) (2020).
[63] F. Gao, A. Bermak, S. Benchabane, L. Robert, A. Khelif, Acoustic radiation-free surface phononic crystal resonator for in-liquid low-noise gravimetric detection, Microsyst. Nanoeng. 7 (2021) 8.
[64] Bonhomme J, Oudich M, Djafari-Rouhani B, Sarry F, Pennec Y, Bonello B, et al. Love waves dispersion by phononic pillars for nano-particle mass sensing. Applied Physics Letters. 2019;114:013501.